

Neutral Density Profiles From a Diverted Plasma in Alcator C-Mod

by

Christopher Paul Barrington-Leigh

Submitted to the Department of Physics
in partial fulfillment of the requirements for the degree of

Bachelor of Science in Physics

at the

MASSACHUSETTS INSTITUTE OF TECHNOLOGY

June 1995

© Massachusetts Institute of Technology 1995. All rights reserved.

Author
Department of Physics
May 12, 1995

Certified by
John E. Rice
Research Scientist, MIT Plasma Fusion Center
Thesis Supervisor

Accepted by
Aron Bernstein
Department of Physics Undergraduate Theses Coordinator

Neutral Density Profiles From a Diverted Plasma in Alcator C-Mod

by

Christopher Paul Barrington-Leigh

Submitted to the Department of Physics
on May 12, 1995, in partial fulfillment of the
requirements for the degree of
Bachelor of Science in Physics

Abstract

The distribution of neutral hydrogen within a tokamak plasma is studied. Soft x-rays observed by the HIREX spectrometer on the Alcator C-Mod tokamak reveal spectral lines due to transitions in excited Ar^{16+} which are preferentially populated by charge exchange recombination between Ar^{17+} and neutral hydrogen. Three simple models for the spatial cross-sectional distribution of neutral hydrogen are used to predict spectral charge exchange signals, and the results are compared with experimental observations. An up-down asymmetry of neutral hydrogen density is confirmed, and explained in terms of the open field lines and divertor plate at the bottom of the tokamak.

Thesis Supervisor: John E. Rice

Title: Research Scientist, MIT Plasma Fusion Center

Acknowledgments

To Nancy Norwood, Linda Fortin, and Grant Cameron,
for showing me excellence.

Contents

1	Introduction	8
2	Relevant Atomic Physics	10
2.1	QM of 2-electron Atoms	10
2.1.1	<i>S</i> - States	10
2.1.2	Radiative Transitions	12
2.2	Coronal Equilibrium	13
2.3	Argon in Alcator C-Mod	14
2.3.1	Impurities	14
2.3.2	Ionization Equilibrium of Argon	15
2.4	Population of the $1s^1np^1 - ^1P$ States	17
2.4.1	Radiative Recombination	18
2.4.2	Electron Impact Excitation	19
2.4.3	Charge Exchange Recombination	19
2.4.4	<i>n</i> -Dependence of Population Rates	20
3	Experiment and Models	22
3.1	HIREX Spectra	22
3.2	Predicting Spectra From Profiles of Neutral H Density	24
3.3	Hypotheses for Neutral Density Profiles	26
3.3.1	Symmetries	26
3.3.2	Up - Down Asymmetry	26
3.3.3	Two Dimensional Models	27
4	Results	29
4.1	Neutral H Profiles	29
4.2	Discussion	35
5	Summary	39
A	Charge Exchange Recombination Rate Coefficient	41

List of Figures

2-1	Ionization and recombination rate coefficients versus temperature, shown for Ar^{16+}	15
2-2	Calculated coronal equilibrium populations of Ar charge states as a function of equilibrium temperature, which ranges from 2600 eV at the center of the plasma to 0 at the edge.	16
2-3	Calculated Ar charge states based on ionization, recombination, and transport processes.	17
2-4	A portion of the $1s^1n^1 - ^1P \rightarrow 1s^2$ spectrum with clearly resolvable lines in the range $n = 6$ to $n = 14$. Little or no enhancement of the $n = \{9, 10\}$ lines is evident: the brightnesses fall off roughly as $1/n^3$	18
2-5	Rate coefficients for three processes which populate the $1s^1np^1 - ^1P$ state in Ar^{16+} , showing the different dependences on the level n	20
2-6	n -level dependence (diamonds and triangles) of the rate coefficient for radiative recombination of Ar^{17+} for two values of the electron temperature. The solid curves are $1/n^3$ -shaped and pass through the value for $n = 6$. The discrepancy between the calculated rates and the $1/n^3$ approximations is significant, especially when compared with a small charge exchange signal, and is temperature - dependent.	21
3-1	Cross-section through the plasma (TOP) showing the viewing angles of the HIREX chords for a particular plasma discharge. The signal observed is plotted vs. spectral line for three of the chords (BOTTOM). The dashed line is a $\frac{1}{n^3}$ fit through the $n = 6$ datum.	23
3-2	The FRANTIC density profiles considered. Each is identified by its value at the plasma edge.	28
4-1	Optimization of the “flat” [H] profile for $n = 10$. The vertical bars represent \pm the standard deviation of the discrepancy. (See Section 4.1)	30
4-2	Optimization of the “split-FRANTIC” [H] profile for $n = 10$. The vertical bars represent \pm the standard deviation of the discrepancy (See Section 4.1).	31
4-3	Optimization of the “FRANTIC+cloud” [H] profile, varying both the width and the peak density of the cloud, for $n = 10$. The $1/e$ cloud widths plotted are 2 cm, 6 cm, 10 cm, 20 cm, 30 cm, 40 cm, and 100 cm. The standard deviations of discrepancy are not shown on the plot.	32

4-4	Cross-section through the [H] profiles for each of the three models used. The cross-section is along major radius 0.68 m (see Figure 3-1). The dotted lines show the two components of the FRANTIC+cloud distribution.	33
4-5	One - dimensional neutral profiles determined from matching a model to each of the scanned chord locations. Chords 1, 4, and 5, are plotted with squares, triangles, and asterisks, respectively.	34
4-6	Locations of maximum charge exchange signal for the best fits to each chord position. Chords 1, 4, and 5, are plotted with squares, triangles, and asterisks, respectively.	36
4-7	Correlation between a simple measurement of chord position (squares) and the location of peak emissivity (solid lines).	38

List of Tables

4.1	Summary statistics for the three [H] models examined, based on predictions for $n = 10$. The means and standard deviations shown are calculated over the 22 viewing chords seen by spectrometers 1 and 5 throughout the 11 discharges. Densities are in m^{-3}	35
4.2	Quantity of data from 3 chords and 11 plasma discharges, tabulated according to shot and n-level. The number in parentheses is the percentage of data for which the difference in Equation 3.7 was negative.	37

Chapter 1

Introduction

Research efforts towards achieving magnetically-confined thermonuclear fusion suitable for commercial power generation have made great progress in increasing the plasma density, temperature, and confinement – and thus the evolved energy – in tokamaks. Still comparatively lacking, on the other hand, is experimental demonstration of ways to extract the heat and reaction products from the tokamak.

One effort towards this end involves the use of a “divertor plate” onto which the outermost field lines are directed, concentrating hot ions onto a small region. One way this can succeed in removing heat from the plasma is through radiation given off by charge exchange recombination between impurities and neutrals near the divertor. This radiated energy will then be freed from the plasma, and distributed evenly over the walls of the tokamak.

In order to reach this ideal, the MIT experimental tokamak Alcator-C-Mod is equipped with a divertor at the bottom of the machine. The plasma edge can be directed into this region (“diverted mode”) or kept away from it (“limited mode”). In order to study and develop the possibility of using localized charge exchange recombination to extract fusion energy, the density of neutrals in the plasma and especially around the divertor must be measured.

This work examines the density of neutral hydrogen and its spatial variation in the diverted mode. Previous research has suggested the existence of a large asymmetry in the neutral density in the top and bottom of the tokamak during diverted discharges [3]. These results were based on a one-dimensional model of the neutral density distribution and experimental results. The current work extends this analysis to consider two-dimensional distributions of neutral density and to compare them with results from a large set of data acquired during a dedicated run in 1995.

Light from argon-hydrogen charge exchange recombination viewed by the HIREX spectrometer array was used as a diagnostic for the neutral hydrogen density. The predictions from three different model distributions of neutral hydrogen were compared with experimental spectra.

Chapter 2 describes some basic phenomena of atomic processes in Ar^{17+} and Ar^{16+} , including the ionization, recombination, and excitation processes important to the spectra observed. Chapter 3 covers the form of the experimental data and the methods used to predict spectra from models of neutral hydrogen density profiles. Chapter

4 discusses the results and problems with the models. Chapter 5 summarizes the conclusions obtained and provides some suggestions for future work.

Chapter 2

Relevant Atomic Physics

2.1 QM of 2-electron Atoms

2.1.1 S - States

Some properties of 2-electron systems which will prove significant for the spectra observed in this work follow from basic quantum mechanical considerations. The form of the general state of two spin- $\frac{1}{2}$ particles can be written

$$\Psi(\mathbf{r}_1, \mathbf{r}_2) = \sum_i a_i \psi_i(\mathbf{r}_1, \mathbf{r}_2) \phi_i, \quad (2.1)$$

where the squared modulus of the wavefunction $\Psi(\mathbf{r}_1, \mathbf{r}_2)$ corresponds, as usual, to the probability density of finding the two electrons at positions \mathbf{r}_1 and \mathbf{r}_2 , respectively. The sum in Equation 2.1 is carried out over all of the normalized eigenfunctions $\psi_i(\mathbf{r}_1, \mathbf{r}_2)$ which solve the system's spatial Schrödinger equation. The ϕ_i are the normalized spin states corresponding to each term in the sum, and the a_i are complex coefficients satisfying the normalization condition for Ψ : $\sum_i |a_i|^2 = 1$. In the case of two electrons in the Coulomb potential of a nucleus Z , the $\psi_i(\mathbf{r}_1, \mathbf{r}_2)$ are eigenvalues of the Hamiltonian in the Schrödinger equation ¹

$$\hat{H}\psi = \left[(\hat{p}_1^2 - \frac{Ze^2}{|\mathbf{r}_1|}) + (\hat{p}_2^2 - \frac{Ze^2}{|\mathbf{r}_2|}) + \frac{e^2}{|\mathbf{r}_1 - \mathbf{r}_2|} \right] \psi = E\psi \quad (2.2)$$

where \hat{p}_k is the momentum operator for electron k .

If the solution $\psi_i(\mathbf{r}_1, \mathbf{r}_2)$ has energy eigenvalue E , then due to the perfect symmetry between \mathbf{r}_1 and \mathbf{r}_2 in the Schrödinger equation (2.2), the function $\psi_i(\mathbf{r}_2, \mathbf{r}_1)$ (generated by exchanging \mathbf{r}_1 and \mathbf{r}_2) also solves Equation 2.2 and also has the eigenvalue E . Moreover, excluding the possibility of degenerate eigenvalues (for which this argument is more complicated: see [1, p. 119]), the dimension of the eigenspace associated with eigenvalue E is 1. Therefore the two eigenfunctions $\psi_i(\mathbf{r}_1, \mathbf{r}_2)$ and $\psi_i(\mathbf{r}_2, \mathbf{r}_1)$ are elements

¹Equation 2.2 is the nonrelativistic form, neglecting spin-orbit and finer-structure terms which become important perturbations for high- Z nuclei.

of the same 1-dimensional vector space:

$$\psi_{i(\mathbf{r}_2, \mathbf{r}_1)} = \chi \psi_{i(\mathbf{r}_1, \mathbf{r}_2)}$$

for some $\chi \in C$. Exchanging parameters once again, one finds

$$\psi_{i(\mathbf{r}_1, \mathbf{r}_2)} = \chi^2 \psi_{i(\mathbf{r}_2, \mathbf{r}_1)}$$

and thus $\chi = \pm 1$. Thus, based only on the symmetry in Equation 2.2, we conclude that the spatial component of the wavefunctions are all symmetric or antisymmetric.

Because the two electrons are indistinguishable fermion particles, another restriction follows. According to the Pauli exclusion principle, the overall state Ψ of the two electrons will also be symmetric or antisymmetric, and thus, since the $\{\psi_{i(\mathbf{r}_1, \mathbf{r}_2)}\}$ are mutually orthogonal, each of the spin components ϕ_i of Equation 2.1 can in turn only be symmetric or antisymmetric. The spin components of the two electrons span a 4-dimensional space. By choosing a direction \mathbf{z} and notating the state with the \mathbf{z} -component of spin “up” in the first electron and “down” in the second as ϕ^{+-} , and so forth, a basis consisting only of symmetric and antisymmetric vectors can be constructed as follows:

$$\begin{aligned} S^+ &\equiv \phi^{++} && (\text{symmetric}, S = 1) \\ S^- &\equiv \phi^{--} && (\text{symmetric}, S = 1) \\ S^O &\equiv \frac{1}{\sqrt{2}}[\phi^{+-} + \phi^{-+}] && (\text{symmetric}, S = 1) \\ S^P &\equiv \frac{1}{\sqrt{2}}[\phi^{+-} - \phi^{-+}] && (\text{antisymmetric}, S = 0) \end{aligned}$$

Spatial wavefunctions which are antisymmetric will be multiplied by a spin wavefunction consisting of a superposition of the the symmetric functions S^+ , S^- , and S^O , above. Spatial wavefunctions which are symmetric must have S^P as a spin factor. The former will necessarily have a combined spin of magnitude 1, and the latter a combined spin of magnitude 0. Because He spectra reveal a fine-structure splitting due to spin - orbit coupling for the $S = 1$ states, they are referred to as “triplet” states, while the $S = 0$ states are “singlet.”

Beyond these general considerations, details of the level scheme of heliumlike systems follow from perturbation analysis and numerical techniques, explained in [1]. It turns out that the energy of any state in which both electrons are excited is greater than the ground state energy of a He^+ ion plus a free electron. The doubly-excited states therefore lie in the continuum and bear a much higher probability of undergoing autoionization than relaxation to a bound He-like state: they do not contribute to discrete spectra.

The remaining states have at least one of the electrons in the ground state, and can therefore be conveniently named according to the quantum numbers of their upper electron. For every set of quantum numbers n, l, m except for the ground state, there exists both a singlet and a triplet level, and it turns out that they are not degenerate:

the singlet states are always slightly higher energy than their triplet counterparts. The ground state has a manifestly symmetric spatial distribution, and is thus a singlet state.

2.1.2 Radiative Transitions

Based on the properties outlined above, as well as a number of results from quantum electrodynamics, predictions for the spectra of He-like atoms can be made.

Transitions between atomic levels occur during interactions with photons and with other particles. The former, radiative transitions, are governed by a set of “intercombination selection rules.” These are derived based on a dipole approximation and are well corroborated by experimental evidence, since the vast majority of radiative transitions are electric dipole transitions [1, p. 252]. Where L is the total electronic orbital angular momentum number, S is the total electronic spin angular momentum number, and J is the total electron angular momentum number, small atoms are found to obey the following during a radiative transition:

$$\Delta L = \pm 1$$

$$\Delta S = 0$$

$$\Delta J = 0, \pm 1$$

In addition, transitions between two states which both have $J = 0$ are not allowed.

The third rule above is rigorously obeyed for all atoms in photon emission and absorption transitions. The first two selection rules, on the other hand, are approximations valid for atoms of low atomic number. In atoms with large nuclei and correspondingly small orbital radii, the spin-orbit interaction becomes significant. As a result, the orbital angular momentum L and the spin angular momentum S are no longer each a good quantum number; in classical terms, they are not constants of motion. Accordingly, formally “forbidden” spectral lines are observed for larger atoms, and they become stronger, relative to the allowed lines, like the fifth power of the atomic number [4, p. 103].

The selection rules have very important consequences for the spectra of He-like (two-electron) atoms. For example, a He atom in its ground state has the configuration $1s^2$. Since $L = 0$, the first rule ensures that a simple photon-atom interaction must leave the He in an $L = 1$ state — also called a P state. In addition, since $S = 0$ in the filled orbital of $1s^2$, a photon excitation must lead to the state $1s^1np^1 -^1P$ for some n , rather than $1s^1np^1 -^3P$. In fact, all radiative transitions to or from the ground state must be to or from an $S = 0$ state; for instance, He atoms left in a $1s^12p^1 -^3P$ state from particle collisions cannot undergo direct radiative decay at all. The spectra of low- Z He-like species are therefore split into two completely independent energy-level structures – the singlet levels and the triplet levels – which do not combine optically with one another. In the case of higher- Z He-like ions such as Ar^{16+} , the spin selection rule does not hold rigorously, and for instance the $1s^12p^1 -^3P$ state does decay radiatively to the ground state. However, as mentioned in Section

2.1.2, the energies of triplet levels are noticeably lower than those of their singlet counterparts, and the transitions $1s^1 2p^1 -^3P \rightarrow 1s^2$ and $1s^1 2p^1 -^1P \rightarrow 1s^2$ are easily resolved [2, Table I].

The rates for radiative transitions within the discrete spectrum of He-like species can be calculated numerically from quantum electrodynamics [1]. For the purposes of the calculations needed for this work, however, it suffices to assume that all singlet states, once excited, decay on a very short time scale compared with any other relevant processes. This will allow the equation of state population rates to photon emission rates.

Finally, the radiative transition selection rules are not followed in general for particle-atom collisions, allowing a broader range of states to be populated in electron-ion interactions.

2.2 Coronal Equilibrium

Coronal equilibrium refers to the equilibrium between ionization and recombination processes in the case when diffusion rates of ionic species are negligible. This diffusion condition turns out not to be satisfied for most species in tokamaks; however, as an approximation it is useful for examining qualitative behaviour and determining the dominant ionic species.

Without the diffusion condition, but assuming a circularly-symmetric plasma, a typical model of ionic equilibrium considers only those ionization and recombination processes resulting from ion-electron collisions.² In addition, reactions which change an ion's charge state by more than ± 1 are neglected. Defining $[Z_q]$ to be the concentration of an atom of nuclear charge Z and overall charge $+q$; S_q to be the electron collision ionization rate coefficient for the process $Z_q \rightarrow Z_{q+1}$; and α_q^T to be the total electron recombination rate coefficient for the process $Z_q \rightarrow Z_{q-1}$, it follows that [5, p. 1600]

$$\frac{\partial [Z_q]}{\partial t} = -\frac{1}{\rho} \frac{\partial(\rho [Z_q] v_{Z_q})}{\partial \rho} + N_e \left(S_{q-1} [Z_{q-1}] - S_q [Z_q] + \alpha_{q+1}^T [Z_{q+1}] - \alpha_q^T [Z_q] \right). \quad (2.3)$$

Here, the first term on the right hand side is the divergence of the flux density — in other words the contribution from convection and diffusion of the species Z_q . ρ is the radial coordinate, and N_e is the local electron density. The problem thus consists of $Z + 1$ coupled equations, with q ranging from 0 to Z , and with the reasonable condition that $S_Z = \alpha_0 = 0$. When the flux terms are negligible, however, these equations describe coronal equilibrium and are greatly simplified. Multiplying by $\frac{1}{N_e}$ and imposing the equilibrium condition that $\frac{\partial [Z_i]}{\partial t} = 0$, the equations lend themselves

²Cation-cation collisions are typically not energetic enough to effect the exchange of electrons, although ion-proton collisions are sometimes considered [5, p. 1600]. Charge-exchanging collisions between neutral species and ions will be discussed below, but are not significant in determining the charge state densities, except in relatively cold plasma.

to matrix form:

$$\begin{pmatrix} -S_0 & \alpha_1 & 0 & 0 & \cdots \\ S_0 & -(S_1 + \alpha_1) & \alpha_2 & 0 & \cdots \\ 0 & S_1 & -(S_2 + \alpha_2) & \alpha_3 & \cdots \\ 0 & 0 & S_2 & -(S_3 + \alpha_3) & \cdots \\ 0 & 0 & 0 & S_3 & \cdots \\ \vdots & \vdots & \vdots & \vdots & \ddots \end{pmatrix} \begin{pmatrix} [Z_0] \\ [Z_1] \\ [Z_2] \\ [Z_3] \\ \vdots \end{pmatrix} = 0$$

The ratios between consecutive charge states follow immediately from simple row operations: by adding each row to that below it, one finds

$$\frac{[Z_{q+1}]}{[Z_q]} = S_q / \alpha_{q+1}^T. \quad (2.4)$$

The S_q and α_q are usually derived from theoretical calculations, sometimes mixed with some empirical results. These equations will be applied to the case of argon, and the results compared with those of a calculation which takes transport into account.

2.3 Argon in Alcator C-Mod

2.3.1 Impurities

“Impurities” in tokamaks consist of all the wanted and unwanted species other than the fusion reactants and products. Line radiation from heavy impurities can completely drain the confined energy of a plasma: ignition of D-T plasmas can be prevented by the presence of only 3% of low-Z elements (e.g. oxygen) or 0.1% of high-Z elements (e.g. tungsten) [5, p. 1599]. Even so, impurities are invaluable as diagnostic tools for determining a number of plasma parameters. Argon, for instance, is very valuable for the current study for several reasons. Being a noble gas and naturally rare, argon is essentially absent in plasmas to which it has not been purposely added, so its concentration is easily controlled. In addition, and as detailed below, a single charge state of argon (the He-like Ar^{16+}) is present and even dominant under equilibrium conditions over almost the entire temperature range of a typical plasma experiment. This is an attractive condition because it means that spectral lines due to Ar^{16+} states are visible from all locations of the plasma, and because heliumlike spectra have been fairly well studied. The next highest charge state, Ar^{17+} , reacts with neutral hydrogen³ through charge exchange recombination and produces an x-ray line which can be used to determine the local neutral density. Argon is also convenient because a number of prominent spectral lines – and in particular the emissions from this charge exchange recombination – fall within the soft X-ray range accessible to the HIREX spectrometer array on the Alcator C-Mod tokamak at the MIT Plasma

³In practice, plasmas are run with deuterium or deuterium and tritium rather than hydrogen; however, their cross-sections for charge exchange are nearly identical, and hereafter “hydrogen” and “H” will refer to the neutral form of *all* of hydrogen’s isotopes.

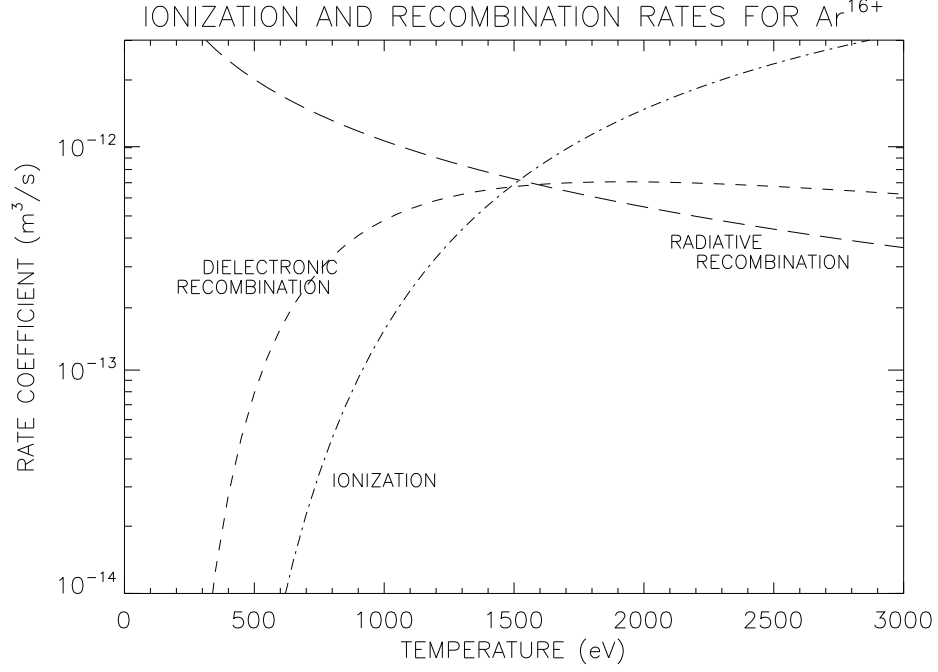


Figure 2-1: Ionization and recombination rate coefficients versus temperature, shown for Ar^{16+} .

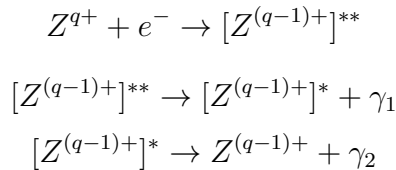
Fusion Center (see Section 3.1).

2.3.2 Ionization Equilibrium of Argon

Using equation 2.4, the relative charge state densities of argon ions under coronal equilibrium can be calculated. Expressions for electron impact ionization and recombination coefficients S_q and α_q^T for the highest charge states of argon are found in [7] and [5]. The dominant recombination processes contributing to α_q^T are radiative recombination:



where the * denotes an electron in an excited state and γ indicates a radiated photon, and dielectronic recombination:



where ** indicates that both the incoming electron and one of the previously-bound electrons finishes in an excited state.

As shown in Figure 2-1, dielectronic recombination of Ar^{16+} becomes important only in hot (core) plasma. The ionization rate shown for Ar^{16+} also suggests that the

population of Ar^{17+} should fall off rapidly towards the edge of the plasma.

The coefficients for ionization, radiative recombination, and dielectronic recombination, when calculated for each of the highest 5 charge states of Ar, lead to the fractional populations shown in Figure 2-2.

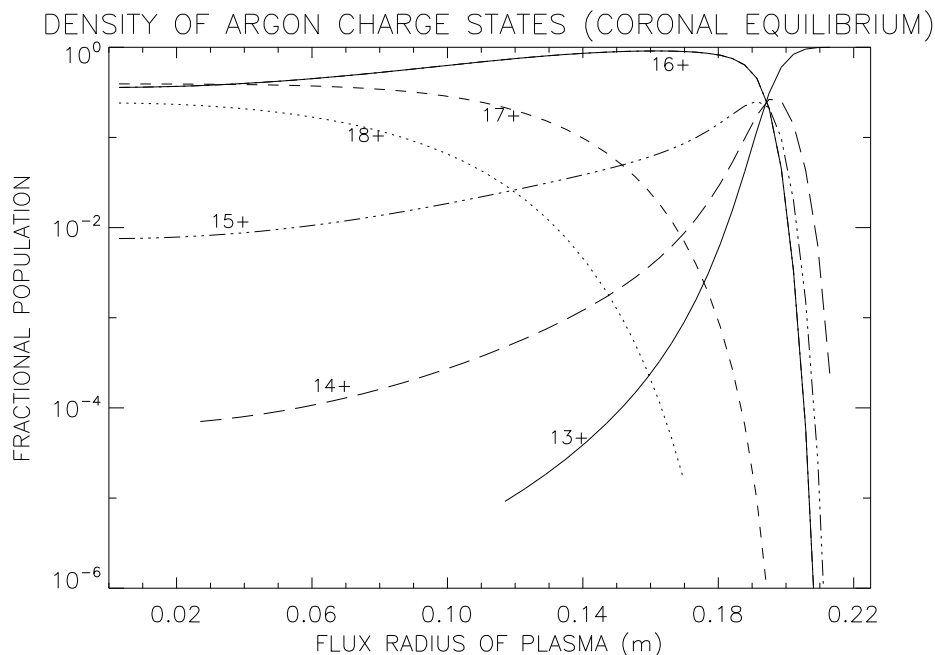


Figure 2-2: Calculated coronal equilibrium populations of Ar charge states as a function of equilibrium temperature, which ranges from 2600 eV at the center of the plasma to 0 at the edge.

Because the populations were calculated assuming Ar^{13+} to be the lowest charge state, they are only accurate where the population of Ar^{13+} is small, or down to about 300 eV. Above this temperature and up to almost 2600 eV – the core temperature in the plasmas used for this work – Ar^{16+} is the dominant charge state of argon.

It has been shown that a coronal model for Ar in a tokamak is inappropriate, since the radial transport timescale is often less than the mean recombination time, and in fact also less than calculated neoclassical predictions [2, p. 3036]. This effect is particularly important near the cooler edge of the plasma. Accordingly, a code to calculate Ar charge state densities based on the full ionization, recombination, and transport model (Equation 2.3) has been developed [3, p. 753]. This code, MIST, uses electron density and temperature profiles determined from other diagnostics to calculate impurity density profiles for each plasma shot. Based on experimental findings, the value used for the flux density $[Z_q]v_{Z_q}$ consisted of a diffusion term and a convection term:

$$[Z_q]v_{Z_q} = 5000 \frac{\text{cm}^2}{\text{s}} \nabla_\rho [Z_q] + 100 \frac{\text{cm}}{\text{s}} v_{Z_q}.$$

The absolute argon density was calculated based on the core electron density, and

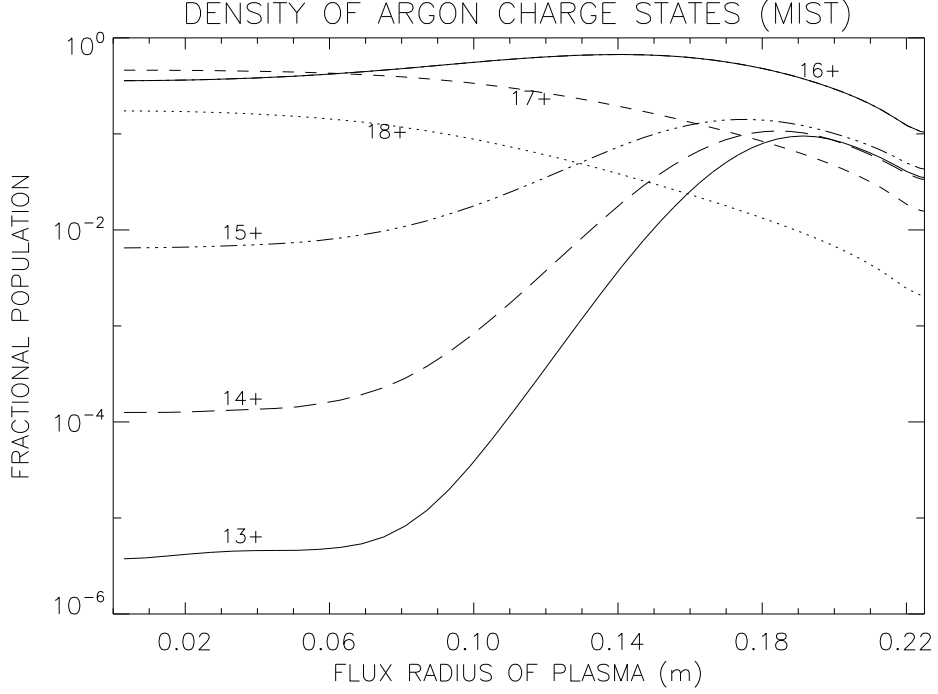


Figure 2-3: Calculated Ar charge states based on ionization, recombination, and transport processes.

a series of calibration shots on Alcator C-Mod [3, pp. 753-754]. The charge state profiles for the essentially identical shots used here are shown in Figure 2-3. The agreement between the profiles from the MIST calculation and those from the coronal approximation is good towards the plasma core. The most significant qualitative difference between them is that, due to rapid transport from the hot core, the populations of Ar^{16+} and Ar^{17+} are still significant near the edge in the case of the MIST profiles.. That this is true experimentally is of great significance because the charge-exchange signal, explained in the next section, depends on the abundances of both Ar^{17+} and neutral hydrogen, which is concentrated mostly at the edge.

2.4 Population of the $1s^1np^1 - ^1P$ States

The HIREX spectrometer is sensitive to the photon energies corresponding to the array of Rydberg transitions $1s^1np^1 \rightarrow 1s^2 + \gamma$ in Ar^{16+} , and has resolved these lines for n in the range 2 to 16 (Figure 2-4). Because of the intercombination selection rules discussed in Section 2.1, these radiative deexcitations only occur from a singlet, $L = 1$ state: 1P . Given also that in a low-density plasma radiative deexcitation occurs almost instantaneously compared with the time between collisions, the rate of photon emission from the above process is simply equal to the rate of excitation to the $1s^1np^1 - ^1P$ states of Ar^{16+} .

These states are populated primarily through radiative recombination of Ar^{17+}

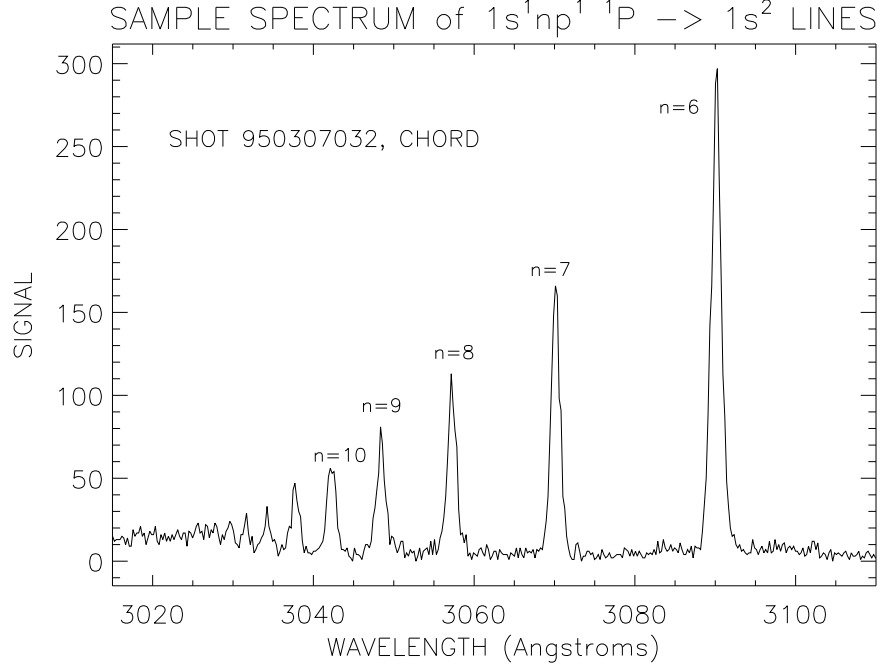


Figure 2-4: A portion of the $1s^1n^1 \text{ } ^1\text{P} \rightarrow 1s^2$ spectrum with clearly resolvable lines in the range $n = 6$ to $n = 14$. Little or no enhancement of the $n = \{9, 10\}$ lines is evident: the brightnesses fall off roughly as $1/n^3$.

, electron impact excitation of ground-state Ar^{16+} , and charge exchange recombination between Ar^{17+} and neutral hydrogen. Dielectronic recombination makes no contribution for reasons outlined in Section 2.1.1.

2.4.1 Radiative Recombination

Radiative Recombination (Equation 2.5) is important both in establishing the ionization equilibrium (see Section 2.2) and in populating the $n^1\text{P}$ levels of Ar^{16+} . Because the recombining electrons have a broad energy distribution compared to the atomic level spacing, the rate of radiative recombination into a level n is proportional simply to the number x of unoccupied orbitals in the level n . Thus $x = 2n^2 - \eta$, where η is the number of electrons in level n . For the rate of radiative recombination into the np orbital only, we set $x = 6$. Then, where T_e eV is the local electron temperature, $g \approx 0.2$ is the free-bound gaunt factor, $q = 17$ for Ar^{17+} , $h\nu$ eV is the ionization energy of the final level n , and $E_1(y)$ is the first-order exponential integral⁴ of y :

$$E_1(y) = \int_1^\infty \frac{1}{z} \exp(-yz) dz, \quad (2.6)$$

⁴An approximation for the first order exponential integral good to within about 1% is given in [7, p. 101].

the rate coefficient for radiative recombination of ground-state Ar^{16+} into the np level is [5, p. 1607]:

$$\langle\sigma v\rangle_{RR}^{nP} = 9.63 \times 10^{-20} \frac{x}{\sqrt{T_e}} g \frac{q^2}{n^3} \frac{h\nu}{T_e} \exp\left(\frac{h\nu}{T_e}\right) E_1\left(\frac{h\nu}{T_e}\right) \text{ m}^3/\text{s}. \quad (2.7)$$

Because the recombining electrons are spin-unpolarized, $\frac{1}{4}$ of the final states will be singlet, so $\langle\sigma v\rangle_{RR}^{n^1P} = \frac{1}{4}\langle\sigma v\rangle_{RR}^{nP}$.

2.4.2 Electron Impact Excitation

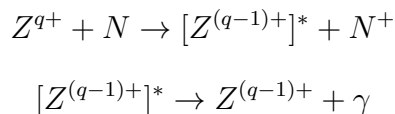
The $1s^1np^1 - ^1P$ state of Ar^{16+} is also populated by excitation from the ground state of Ar^{16+} through collision with an electron. Where T_e eV is the local electron temperature, $h\nu$ eV is the energy difference between the initial and final electron levels, $f_{1,n} = 3.6/n^3$ is the optical oscillator strength between levels 1 and n , and $g \approx 0.2$ is the integrated effective gaunt factor detailed below, the rate coefficient of electron impact excitation of Ar^{16+} with the excited electron ending up in level n is (adapted from [6, p. 216]):

$$\langle\sigma v\rangle_{EXC}^n = 1.58 \times 10^{-11} \frac{1}{\sqrt{T_e}} \frac{f_{1,n} g}{h\nu} e^{-h\nu/T_e} \text{ m}^3/\text{s}. \quad (2.8)$$

Once again it can be assumed that the Ar^{16+} always begins in its ground state. Parameters for a fit to approximate the integrated effective gaunt factor for different n transitions can be found in [6, pp. 216, 219]. Also, screening factors for calculating $h\nu$ are in [7, p. 105].

2.4.3 Charge Exchange Recombination

There is another recombination process not considered in the discussion of ionization equilibrium: charge exchange recombination. It does not significantly shift the equilibrium because its rate is proportional to the density of neutral particles in the plasma. At typical tokamak temperatures, neutral species are very rare unless they are directly injected into the plasma (neutral beam injection). Nevertheless the radiation γ given off by charge exchange recombination with some neutral atom N ,



is detectable and provides a useful diagnostic for determining the density of the neutral species. A noticeable rate of charge exchange recombination occurs in Alcator C-Mod plasmas between Ar^{17+} and neutral hydrogen. The rate coefficient for this process at an ion temperature of T eV, leaving the electron excited in level n of Ar , is [8]

$$\langle\sigma v\rangle_{CX}^n = 2.2 \times 10^{-14} e^{-(n-9.1)^2} T^{0.39} \text{ m}^3/\text{s}. \quad (2.9)$$

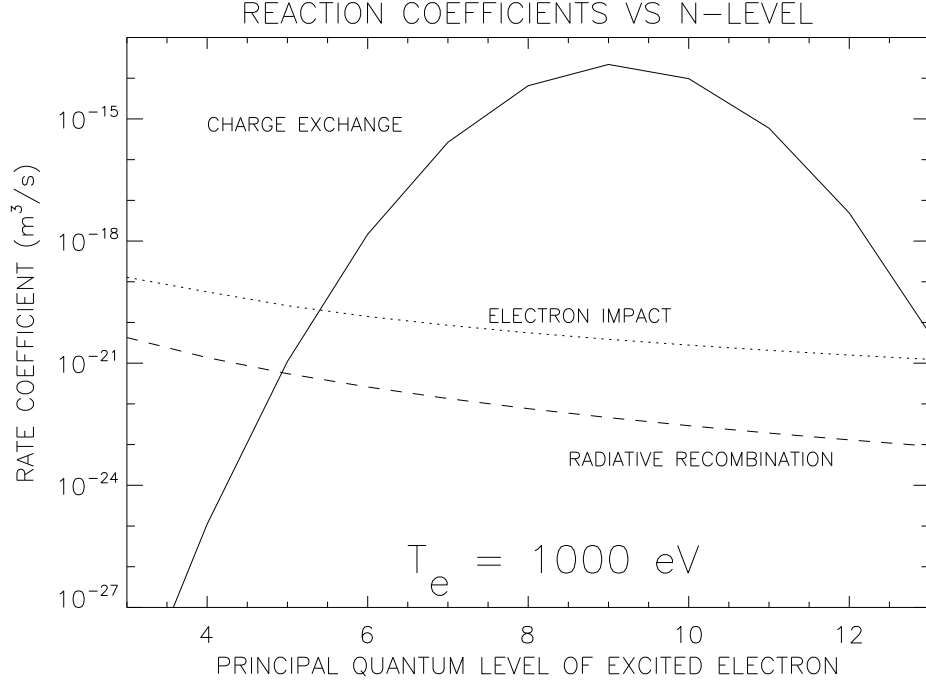


Figure 2-5: Rate coefficients for three processes which populate the $1s^1np^1 -^1P$ state in Ar^{16+} , showing the different dependences on the level n .

Of the reactions leaving an electron in level n , 27% leave the electron in a P level [2, p. 3040]. Of these 1/4 are in a singlet state and 3/4 are in a triplet state. Thus the rate coefficient for charge exchange recombination into the $1s^1np^1 -^1P$ level is $\langle\sigma v\rangle_{CX}^{n^1P} = 0.27 \frac{1}{4} \langle\sigma v\rangle_{CX}^n$.

2.4.4 n -Dependence of Population Rates

As is evident from Figure 2-5, charge exchange between Ar^{17+} and neutral H strongly favours an excited level near $n = 9$. A classical justification for this property is developed in Appendix A. The density profiles of Ar^{16+} , Ar^{17+} , and electrons, as well as the electron temperature profile, can be obtained with considerable confidence [3, 2] from plasma diagnostics and the MIST calculation. Thus, if the distribution of radiative recombination and electron impact excitation rates over different n -levels is known, the contribution of processes other than charge exchange towards a signal which includes charge exchange light can be deduced from the signal due to an n -level for which the charge exchange contribution is known to be minimal (see Section 3.2). For instance, previous studies [2] have deduced the non - charge exchange contribution towards an x-ray signal due to the transition $1s^110p^1 -^1P \rightarrow 1s^2$ by extrapolating from the observed signal due to the $1s^16p^1 -^1P \rightarrow 1s^2$ line. This extrapolation has generally been based on an assumed $1/n^3$ dependence of the radiative recombination and electron impact excitation coefficients. While Equations 2.7 and 2.8 both exhibit a partial dependence on $1/n^3$, their deviation from such a behaviour is significant,

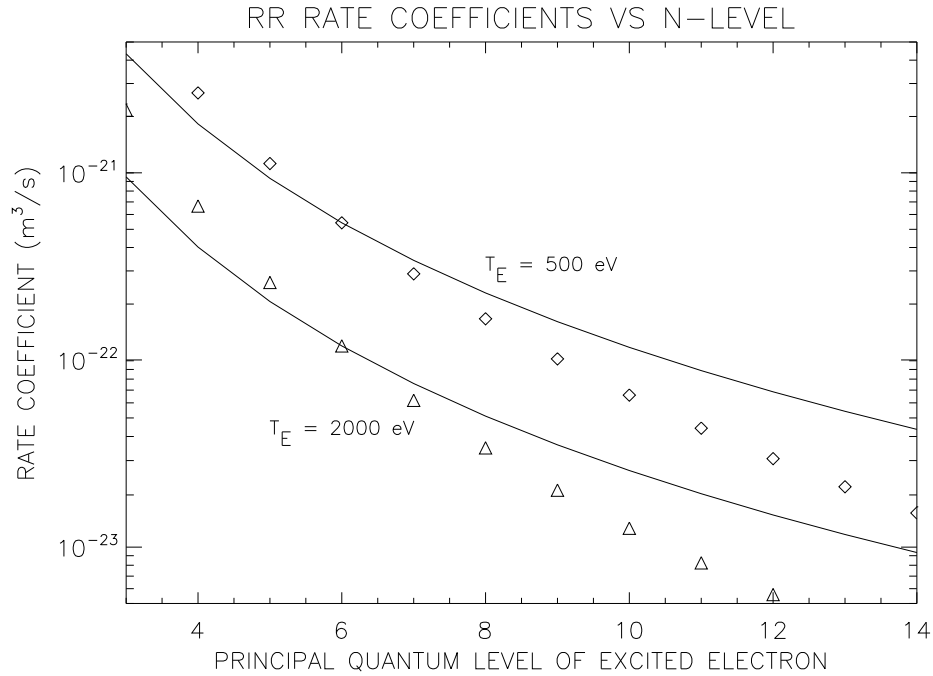


Figure 2-6: n -level dependence (diamonds and triangles) of the rate coefficient for radiative recombination of Ar^{17+} for two values of the electron temperature. The solid curves are $1/n^3$ -shaped and pass through the value for $n = 6$. The discrepancy between the calculated rates and the $1/n^3$ approximations is significant, especially when compared with a small charge exchange signal, and is temperature - dependent.

due to their simultaneous dependence on the n -level energies through $h\nu$. This is especially the case for radiative recombination, as shown in Figure 2-6, where for $n = 10$ the discrepancy is more than a factor of 2.

Chapter 3

Experiment and Models

3.1 HIREX Spectra

The spectra from $1s^1n^1 - ^1P \rightarrow 1s^2$ transitions have wavelengths

$$\begin{aligned}\lambda &= 3.091\text{\AA} \quad \text{for } n = 6 \\ &= 3.038\text{\AA} \quad \text{for } n = 10 \\ &= 3.009\text{\AA} \quad \text{for } n = \infty\end{aligned}$$

in the soft x-ray region. These wavelengths are accessible to the high resolution x-ray spectrometer array (HIREX) installed on the Alcator C-Mod tokamak [3]. HIREX consists of five von Hamos spectrometers, each of which can be independently aimed along a “chord” through the plasma. Each spectrometer can also be tuned for sensitivity to any wavelength range 120 mÅ wide and in between 2.8 Å and 4 Å, and can thus be tuned to view all at once the section of the spectrum ranging from $n = 6$ to $n = 10$. As a measure of the intensity of each spectral line, the product of the height and width of a Gaussian fit was taken. The widths were due to thermal Doppler broadening and instrumental widths. Figure 3-1 shows one set of chord orientations projected onto a plasma cross-section, along with the brightnesses calculated from spectra similar to Figure 2-4 for chords 1, 4, and 5. The spectral data was integrated over approximately one second. A relative enhancement in $n = 9$ and $n = 10$ is evident for chords 1 and 5, which viewed more plasma near the cooler edge and thus saw proportionally more charge exchange signal; however, the absolute signal levels from these cool areas were very small.

The data for this study was provided by 11 plasma discharges, 950307026 - 950307036, from March 7, 1995. The electron temperature and density profiles, the timing of a 60 ms puff of neutral argon, the toroidal field of 5.3 T, and the plasma current of 800 kA were consistent during the “flat-top” of the discharges – between 0.5 and 1.0 seconds after the beginning of the discharge. The electron temperature

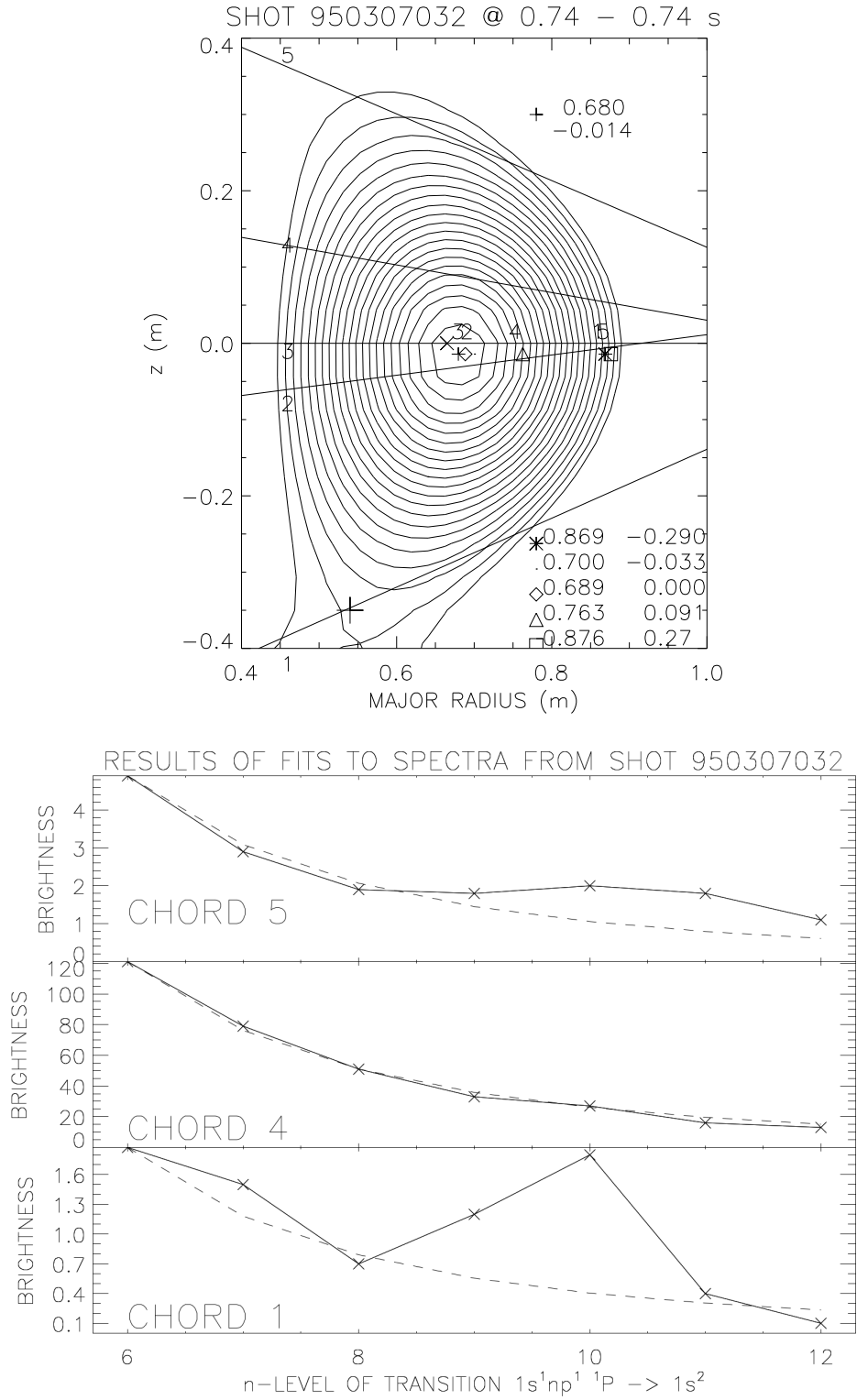


Figure 3-1: Cross-section through the plasma (TOP) showing the viewing angles of the HIREX chords for a particular plasma discharge. The signal observed is plotted vs. spectral line for three of the chords (BOTTOM). The dashed line is a $\frac{1}{n^3}$ fit through the $n = 6$ datum.

and density for this period were well approximated in the integrations by

$$T_e = 2600 \text{ eV} \left[1 - \frac{\rho^2}{(0.225 \text{ m})^2}\right]^{3/2} \quad (3.1)$$

$$[e^-] = 9.0 \times 10^{19} \text{ m}^{-3} \left[1 - \frac{\rho^2}{(0.225 \text{ m})^2}\right]^{0.35} \quad (3.2)$$

where ρ is the radial flux coordinate. For the purposes of evaluating equation 2.9, the ion temperature was assumed to be the same as T_e .

During the 11 discharges, spectrometers 1 and 5 were scanned over the lower and upper regions, respectively, of the plasma, and spectrometer 4 ranged over a more central region. Spectrometers 2 and 3 were kept localized through the center of the plasma and provided a consistency check between shots, confirming that the central argon density was a constant.

3.2 Predicting Spectra From Profiles of Neutral H Density

In principle, the local neutral H density can be calculated from the local electron density if the respective emissivity contributions from H-dependent reactions (charge exchange recombination) and electron-dependent reactions (radiative recombination and collisional excitation) are known [2, p. 3042]. Instead, because the emissivities are not known locally, line integrals of emissivity along the chords sighted by HIREX were carried out, and these results compared to the experimental data in order to evaluate different hypothesized neutral density profiles.

From Section 2.4, the total photon emission rate per volume $e_n(\mathbf{r})$ at position \mathbf{r} from the transition $1s^1n^1 -^1P \rightarrow 1s^2$ is equal to the rate of population of the state $1s^1np^1 -^1P$:

$$e_n(\mathbf{r}) = \langle \sigma v \rangle_{CX}^{n^1P} [\text{Ar}^{17+}] [\text{H}] + \langle \sigma v \rangle_{EXC}^{n^1P} [e^-] [\text{Ar}^{16+}] + \langle \sigma v \rangle_{RR}^{n^1P} [e^-] [\text{Ar}^{17+}] \quad (3.3)$$

where brackets denote density, and each parameter on the right is evaluated locally. Observations yield instead the quantity

$$E_n = \int_{V_c} A_c(\mathbf{r}) e_n(\mathbf{r}) dV, \quad (3.4)$$

where the integration is carried out over the volume V_c viewed by chord c . Here $A_c(\mathbf{r})$ is the sensitivity of the experimental apparatus on chord c , including all geometrical factors and detector gains. $A_c(\mathbf{r}) = A_c$ can be taken out of the integral by assuming that the chord consists of a cylindrical volume, and that the plasma is optically thin, so that the instrument is equally sensitive to x-rays from every region within the chord volume.

Introducing the total argon density $[\text{Ar}]$ summed over all charge states, the cali-

bration factor A can be expressed from Equations 3.3 and 3.4 as

$$A_c = \frac{E_n}{\int_{V_c} [\text{Ar}] \frac{[\text{Ar}^{17+}]}{[\text{Ar}]} (\langle \sigma v \rangle_{CX}^{n1P} [\text{H}] + \langle \sigma v \rangle_{EXC}^{n1P} [e^-] \frac{[\text{Ar}^{16+}]}{[\text{Ar}^{17+}]} + \langle \sigma v \rangle_{RR}^{n1P} [e^-]) dV} \quad (3.5)$$

The *ratios* of argon densities in Equation 3.5 are known with confidence, as is each of the other terms in the equation, except for A_c , $[\text{Ar}]$, and $[\text{H}]$. Assuming that the total argon density $[\text{Ar}]$ is uniform throughout V_c , and can thus be taken out of the integral, then, because of the strong n -dependence of the charge exchange cross-section, an n -level can be found for which $\langle \sigma v \rangle_{CX}^{n1P}$ is negligible, eliminating the first term in the integral of Equation 3.5, and determining a fixed value of the product $A_c[\text{Ar}]$. This “fiducial” level was $n = 6$ for all of the integrations carried out here,¹ as well as for similar work in the past [2]. Thus,

$$A_c[\text{Ar}] = \frac{E_6}{\int_{V_c} \frac{[\text{Ar}^{17+}]}{[\text{Ar}]} [e^-] (\langle \sigma v \rangle_{EXC}^{61P} \frac{[\text{Ar}^{16+}]}{[\text{Ar}^{17+}]} + \langle \sigma v \rangle_{RR}^{61P}) dV}. \quad (3.6)$$

Next, the neutral density profile $[\text{H}]$ can be evaluated by comparing the predicted and observed signal *contributions* due to charge exchange recombination for an n -level where charge exchange is significant (such as $n = 9$ or $n = 10$). The observed charge exchange signal is, with good confidence, the difference between the total observed signal and the portion of it which is expected to come from sources other than charge exchange:

$$E_n^{CX} = E_n - A_c[\text{Ar}] \int_{V_c} \frac{[\text{Ar}^{17+}]}{[\text{Ar}]} [e^-] (\langle \sigma v \rangle_{EXC}^{n1P} \frac{[\text{Ar}^{16+}]}{[\text{Ar}^{17+}]} + \langle \sigma v \rangle_{RR}^{n1P}) dV \quad (3.7)$$

The model charge exchange signal M_n^{CX} , on the other hand, depends on the proposed neutral profile $[\text{H}]$:

$$M_n^{CX} = A_c[\text{Ar}] \int_{V_c} \langle \sigma v \rangle_{CX}^{n1P} \frac{[\text{Ar}^{17+}]}{[\text{Ar}]} [\text{H}] dV \quad (3.8)$$

An agreement between E_n^{CX} and M_n^{CX} indicates the success of the model $[\text{H}]$ distribution. A measure of the consistency between these two values formed the basis of an evaluation of several different candidate neutral density profiles.

¹The contribution of the charge exchange term to the integral for $n = 6$ was uniformly less than 0.02%

3.3 Hypotheses for Neutral Density Profiles

3.3.1 Symmetries

A ubiquitous assumption in tokamak physics is that densities and temperatures are toroidally symmetric. At typical thermal velocities of 10^5 m/s and low enough densities such that the mean free path is comparable to the circumference of the tokamak, equilibrium along toroidal field lines is established on a very short timescale. This assumption has already been implicitly made in the construction and description of the HIREX diagnostic, and limits the task of $[H]$ profile determination to a two-dimensional problem.

Ion and electron properties obey another symmetry for the same reason: on a plot of a plasma cross-section such as Figure 3-1, charged particle properties are also uniform along a *poloidal* field line. In Alcator C-Mod these surfaces are labelled by their intersection ρ with the outer minor radius axis (i.e. by the distance from the plasma center to the right along $Z = 0$ in Figure 3-1). These contour paths are calculated from the plasma current, the toroidal field, magnetic flux data from an array of loops and probes around the plasma, and the equations describing magnetic equilibrium, assuming toroidal symmetry. The “edge” of the plasma is identified by the outer closed flux surface, on which the poloidal symmetry condition breaks down, since charged particles travelling on this field line are ejected at the “X-point” visible at the bottom of Figure 3-1. It is this X-point which is directed onto the divertor plate. The outer closed flux surface for the plasmas considered in this work was the contour $\rho = 0.225$ m.

This poloidal symmetry for charged particles on the closed flux surfaces reduces calculations such as MIST (see Section 2.3.2) as well as descriptions of basic plasma parameters (see Equations 3.1 and 3.2) to one dimension (ρ). For neutral particles, however, the same symmetry does not follow easily. The ionization and recombination processes acting as sources and sinks of neutral hydrogen are functions of charged particle properties, and thus they are well described by functions of ρ alone. The neutrals themselves, however, are not bound to magnetic field lines, and thus their transport and distribution may be more complicated. The deviation of $[H]$ from a ρ -symmetric distribution is discussed in the next two sections.

3.3.2 Up - Down Asymmetry

Assuming symmetries over toroidal position and radial flux surface, theoretical profiles of the H density have been calculated with the FRANTIC neutral transport code [2, 3]. With the specification of other experimentally - determined plasma parameters for a particular discharge, the only free parameter in the FRANTIC calculation is the neutral density at the edge (last closed flux surface) of the plasma.

In a previous study, experimental neutral densities were calculated as a function of vertical position based only on the temperature and densities at the midpoint of each chord [2, 3]. These results were then compared with FRANTIC $[H]$ profiles for a range of edge density values. When based on observations at the top (chord 5) and

the bottom (chord 1), the results suggested profiles that differed by over 100 times at the edge and by more than a factor of 2 at the center. This enhancement of H density near the bottom of the machine, which is evident primarily in diverted plasmas, can be seen directly from the brightnesses in Figure 3-1.

Based on the discussion above, this up-down asymmetry can be anticipated for a diverted plasma as a result of the X-point near the bottom of the tokamak. Ions travelling along the outer flux surface will escape the plasma preferentially at the *bottom* of the tokamak, and will cool down and recombine as they collide with the divertor plate or with the cloud of cold ions and neutrals that has collected there. A reversed up-down asymmetry ought to be observed for plasmas run with the X-point at the top of the tokamak. As outlined in the Introduction, this process of extracting heat from the plasma in the form of radiation from combining ions in a cold “cloud” near the divertor is a desired effect with practical applications. The neutral particles in this cold cloud could then diffuse back into the plasma, resulting in an elevated neutral density over a broad region in the lower part of the tokamak.

3.3.3 Two Dimensional Models

To evaluate better the symmetries and asymmetries of H density discussed above, more data have been acquired (see Section 3.1) and a more sophisticated analysis which takes into account the full two-dimensional dependence of the [H] and other plasma parameters (see Section 3.2) has been carried out. Three classes of model [H] profile were compared with results from the scanned chords 1, 4, and 5. These are described below.

Split-FRANTIC Profiles

As shown in Figure 3-2, [H] profiles were calculated by FRANTIC for a representative discharge from March 7th, 1995 and assuming edge densities of $5 \times 10^{13} \text{ m}^{-3}$ to $1 \times 10^{16} \text{ m}^{-3}$. While the edge densities range over more than two orders of magnitude, the core densities vary by only a little more than a factor of 10.

In order to compare with the previous results mentioned in Section 3.3.2, and despite the unphysical nature of the model, the top and bottom halves (corresponding to data from chords 5 and 1, respectively) of the profile were allowed to vary separately, so the resulting optimized “split-FRANTIC” model was specified by the top and bottom edge densities.

Flat Profiles

In order to have a reference with which to measure the success of the split-FRANTIC model, a series of “flat” profiles were evaluated. These consisted of spatially uniform neutral densities, except that the top and bottom of the profile were again allowed to vary independently, and an optimized profile was constructed from the best fit to the top and the best fit to the bottom.

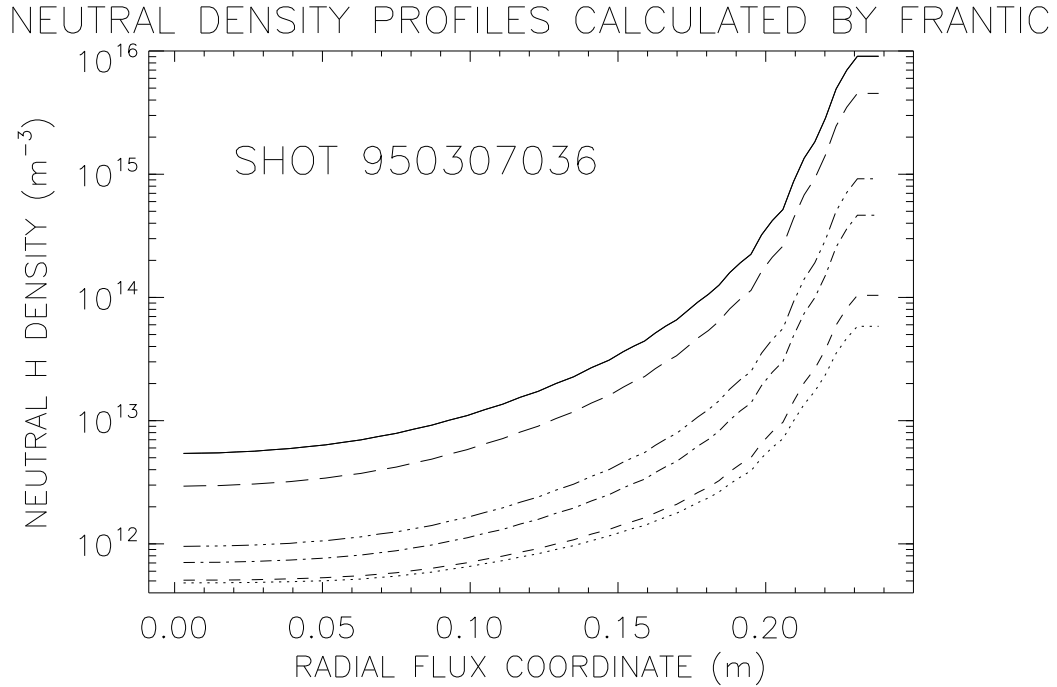


Figure 3-2: The FRANTIC density profiles considered. Each is identified by its value at the plasma edge.

FRANTIC + Cloud Profiles

Based on the hypothesized source of the up-down asymmetry, a “FRANTIC + cloud” model was constructed from a FRANTIC profile plus a Gaussian-shaped distribution centered at a fixed point near the divertor. This point is shown in Figure 3-1 as a + near the x-point at the bottom of the plasma. The peak density and the width of this added-on Gaussian were both allowed to range freely, but the FRANTIC term was fixed to best fit the upper portion of the plasma, where the influence of the divertor and cloud ought to be minimal.

Chapter 4

Results

4.1 Neutral H Profiles

For each of the chords 1, 4, and 5 from each shot, and for every candidate model H distribution, the spatial integrals in Equations 3.6, 3.7 and 3.8 were carried out numerically in 100 slices, assuming a narrow, cylindrical shape of the viewing chords.

Data for which the difference in Equation 3.7 was negative were ignored. This occurrence was rare for $n = 10$ lines, which also had stronger signals than those of $n = 9$ in general (see Table 4.2). For this reason, $n = 10$ was used exclusively in Equations 3.7 and 3.8.

The appropriateness of each fit was evaluated as follows. M_n^{CX} and E_n^{CX} (Equations 3.7 and 3.8) were calculated and their ratio M_n^{CX}/E_n^{CX} taken for each chord. The absolute value of the natural logarithm of this ratio $|\log(M_n^{CX}/E_n^{CX})|$ was averaged over all the orientations of chords 1 and 5 throughout the 11 discharges; this mean will be referred to as the *mean discrepancy*. Thus a mean discrepancy of 0 would imply a perfect agreement between the model and the deductions based on experimental observations. In addition, to evaluate the significance of these mean discrepancies, the standard deviation of $|\log(M_n^{CX}/E_n^{CX})|$ over the different chord locations was calculated.

Figures 4-1, 4-2, and 4-3 display the results from the selection of optimized representatives of each of the three types of model [H] distribution described in Section 3.3.3. The data from chords 1 and 4 agree on the preferred “flat” profile (Figure 4-1) of $2 \times 10^{13} \text{ m}^{-3}$, while the mean discrepancy for chord 5 had its minimum for a neutral density of $0.7 \times 10^{13} \text{ m}^{-3}$. Similarly, chords 1 and 4 both fit best to a split-FRANTIC profile (Figure 4-2) with edge neutral density of $100 \times 10^{13} \text{ m}^{-3}$, while data from chord 5 preferred the lowest-density FRANTIC profile tested, with an edge density of $5 \times 10^{15} \text{ m}^{-3}$. Thus in both cases the anticipated enhancement of the neutral density towards the bottom of the tokamak is evident; however, the neutral density determined for the middle region by chord 4 is considerably higher than expected. This is especially the case in the split-FRANTIC case, as can be seen in Figure 4-2. This consistently-observed result suggests either a higher central neutral density than predicted by FRANTIC, or a systematic error in the sensitivity in spectrometer 4. On

RESULTS FROM FLAT PROFILE

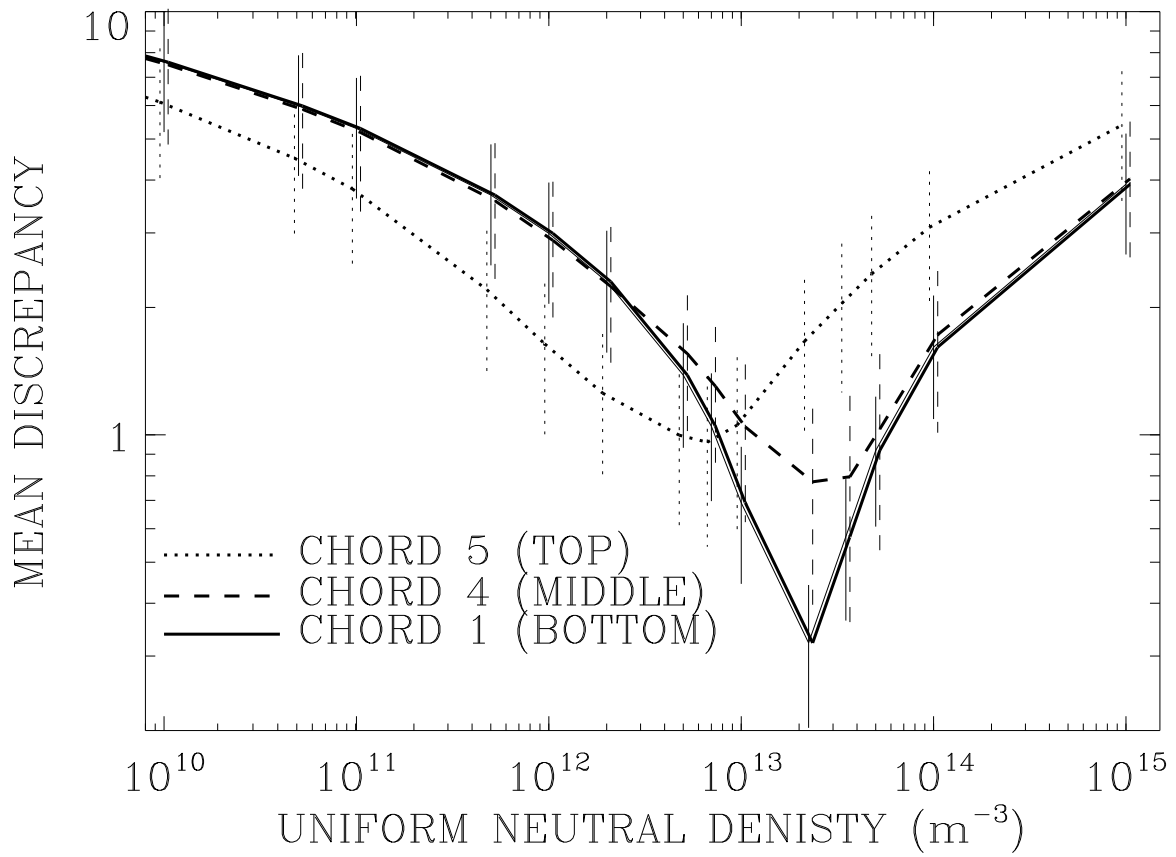


Figure 4-1: Optimization of the “flat” [H] profile for $n = 10$. The vertical bars represent \pm the standard deviation of the discrepancy. (See Section 4.1)

RESULTS FROM FRANTIC PROFILE

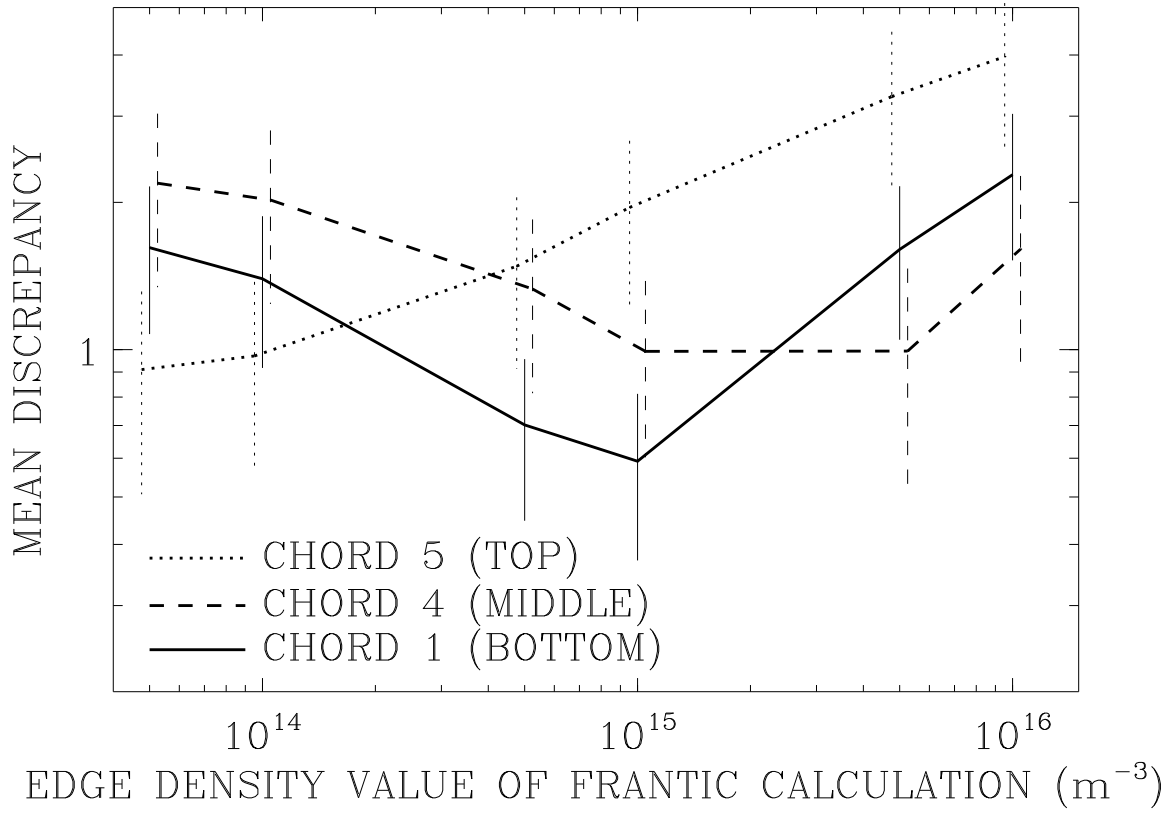


Figure 4-2: Optimization of the “split-FRANTIC” $[H]$ profile for $n = 10$. The vertical bars represent \pm the standard deviation of the discrepancy (See Section 4.1).

RESULTS FROM FRANTIC + CLOUD PROFILE

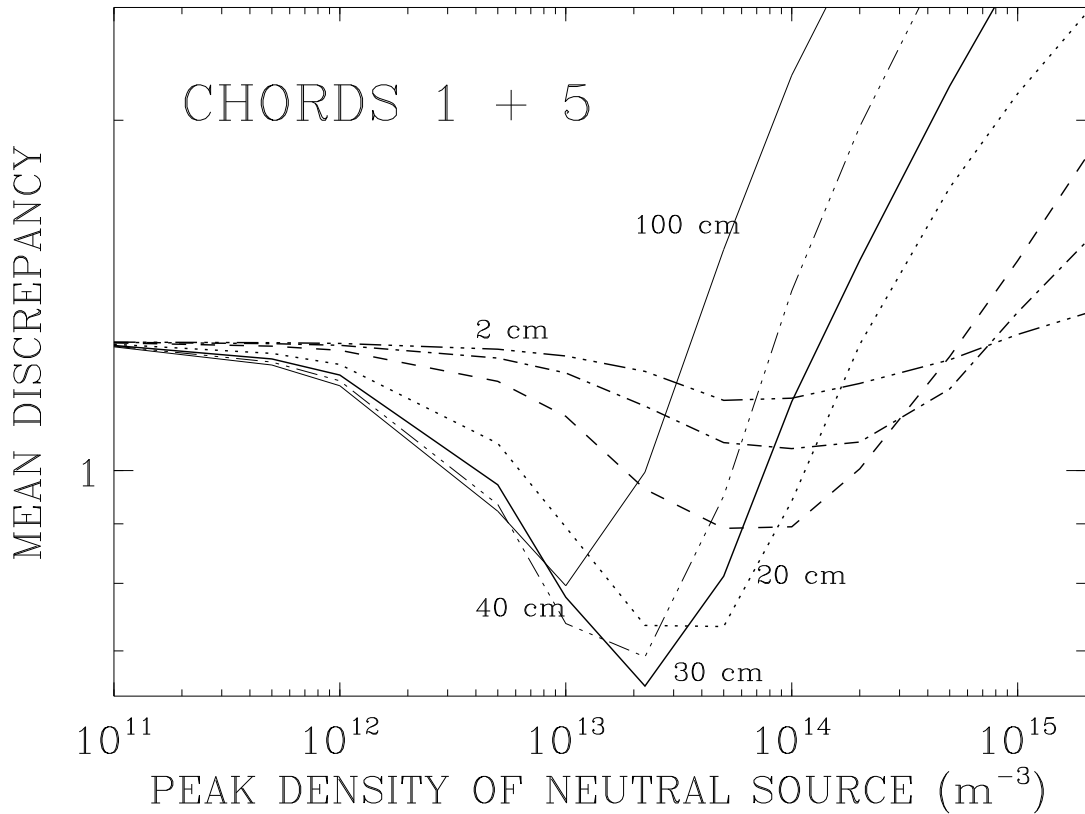


Figure 4-3: Optimization of the “FRANTIC+cloud” [H] profile, varying both the width and the peak density of the cloud, for $n = 10$. The $1/e$ cloud widths plotted are 2 cm, 6 cm, 10 cm, 20 cm, 30 cm, 40 cm, and 100 cm. The standard deviations of discrepancy are not shown on the plot.

VERTICAL CROSSECTION OF THREE NEUTRAL DENSITY MODELS

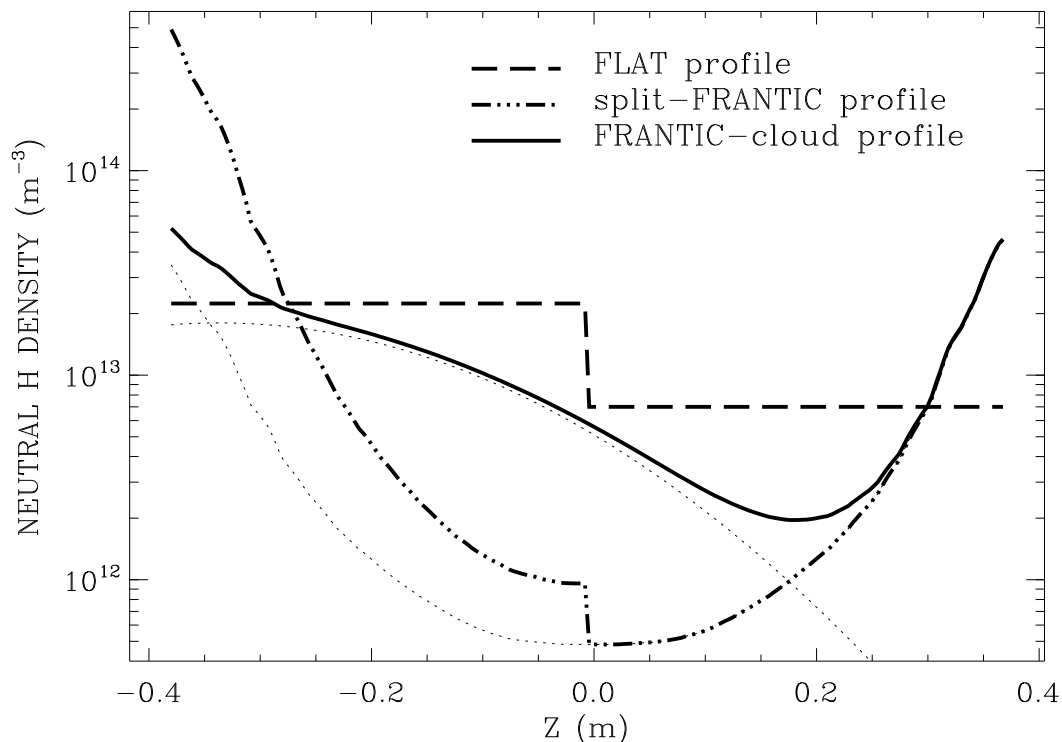


Figure 4-4: Cross-section through the $[H]$ profiles for each of the three models used. The cross-section is along major radius 0.68 m (see Figure 3-1). The dotted lines show the two components of the FRANTIC+cloud distribution.

the latter assumption, chord 4 results were discounted in the final comparison (see Section 4.2).

For the FRANTIC + cloud distribution, a FRANTIC profile with edge density $5 \times 10^{13} \text{ m}^{-3}$ was used, as suggested by the results above for the top of the plasma. Chord 5 integrations were not very sensitive to the size of the cloud, except for large widths of the cloud. Results from chord 1 favoured a broad (30 cm) cloud with an amplitude of $2 \times 10^{13} \text{ m}^{-3}$, as did the combined results of chords 1 and 5.

Neutral densities according to each of the three optimized models along a vertical cross-section through the middle of the plasma are plotted in Figure 4-4, and comparisons of the success of each model are summarized in Table 4.1.

A possibly more direct way of relating the emissivity integrals to neutral densities is to match the optimal profile to each viewing chord location individually. This was done and the results are shown in Figure 4-5. The “locations” are specified by the Z-coordinate (see Figure 3-1) corresponding to the point of maximum charge-exchange emissivity found along each chord. While in both cases the data are suggestive of a peaked neutral density near the plasma edge, the points are scarce and not cohesive.

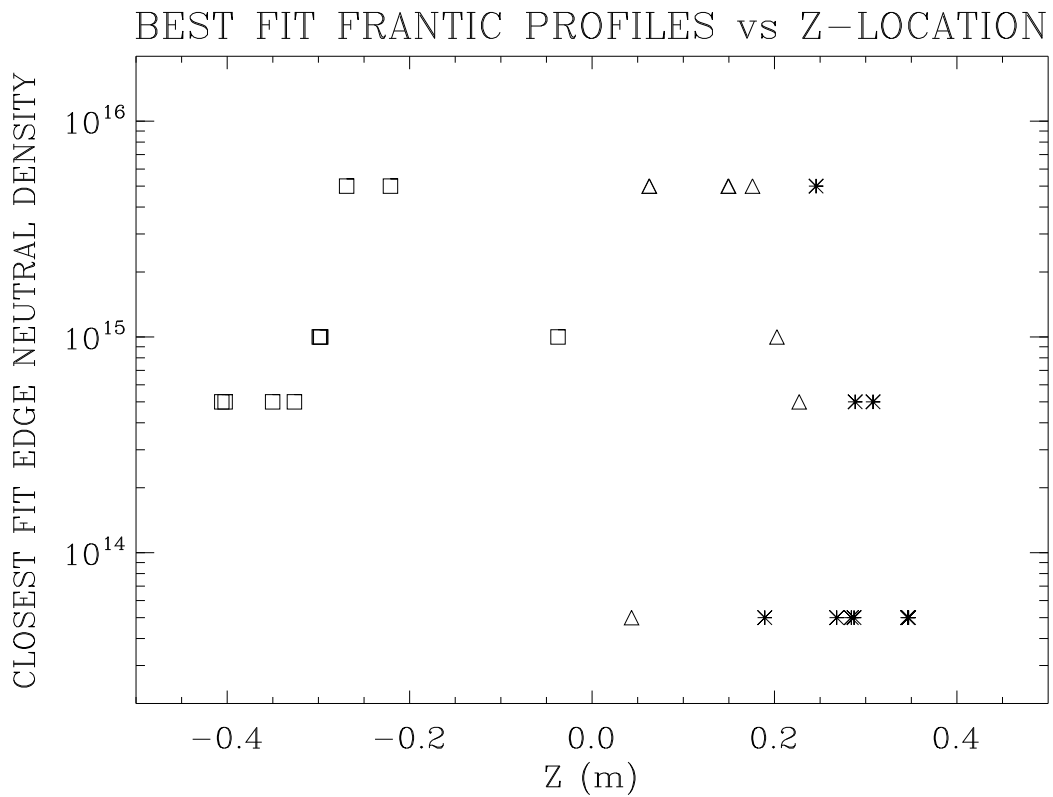
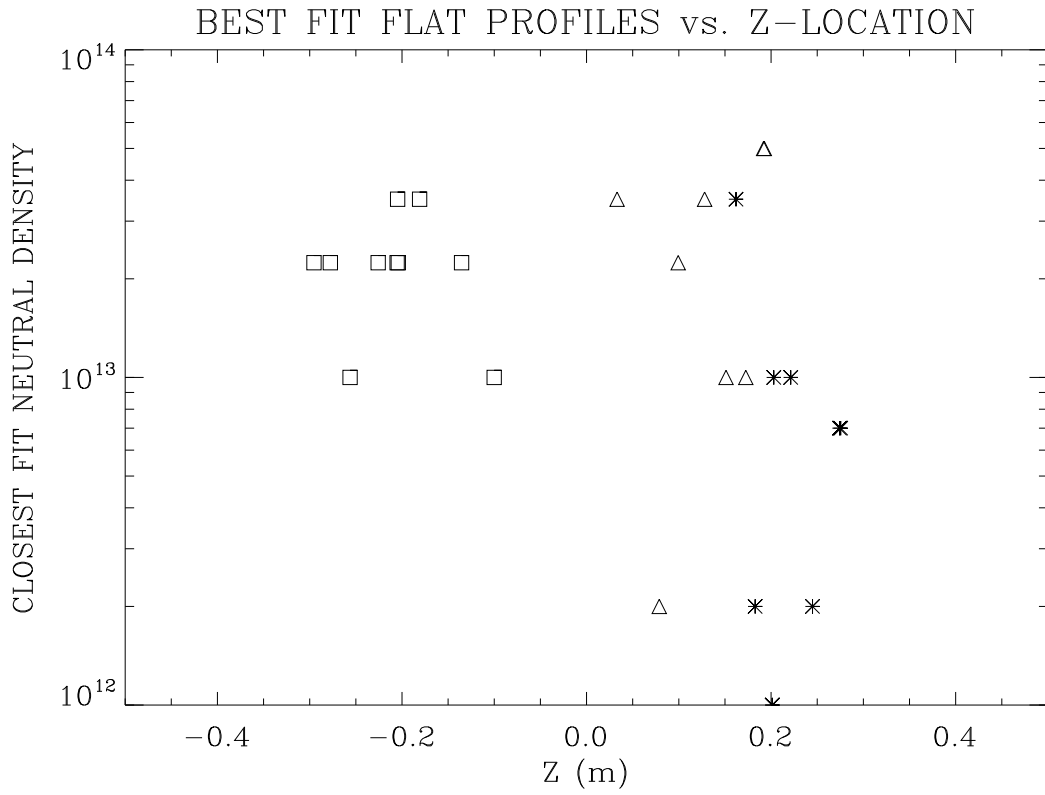


Figure 4-5: One - dimensional neutral profiles determined from matching a model to each of the scanned chord locations. Chords 1, 4, and 5, are plotted with squares, triangles, and asterisks, respectively.

Table 4.1: Summary statistics for the three [H] models examined, based on predictions for $n = 10$. The means and standard deviations shown are calculated over the 22 viewing chords seen by spectrometers 1 and 5 throughout the 11 discharges. Densities are in m^{-3} .

MODEL:	flat	split-FRANTIC	FRANTIC-cloud
Description	uniform densities of 2×10^{13} in the bottom half and 0.7×10^{13} in the top	FRANTIC profiles with top and bottom edge densities of 5×10^{13} and 100×10^{13} , respectively	FRANTIC profile with edge density of 5×10^{13} added to a cloud with peak density 2.2×10^{13} and width 30 cm
Discrepancy (Mean \pm StdDev)	0.64 ± 0.31	0.75 ± 0.32	0.65 ± 0.34

4.2 Discussion

Several difficulties exist with the results as summarized in Table 4.1:

1. Given the large standard deviations in Table 4.1, the results do not discriminate strongly between the three different models. This is troubling because the flat profiles and the FRANTIC profiles are significantly different in qualitative character. Figure 4-6 shows the locations of maximum emissivity for each chord position. For flat profiles and for the broad, high densities in the bottom half of the FRANTIC-cloud distribution, the charge exchange signal comes primarily from the innermost flux surface encountered by each viewing chord. In the case of FRANTIC profiles on the other hand, the charge exchange signal comes mostly from the plasma edge, with another smaller peak in the center of the plasma. That the difference between these two extremes cannot be discerned from the given data suggests a fundamental lack of precision in the calculation. The spectral data used were simply not plentiful and detailed enough to deconvolve the neutral density beyond the one-dimensional asymmetry which is apparent and consistent among the three models in Figure 4-4. The best fit, with an average discrepancy of 0.64, corresponds to a difference (either high or low) of a factor of 1.8 between the observed and calculated charge exchange signals – a significant fraction based on the scales in Figure 4-4.
2. The relative success of the flat profile was especially unanticipated. There are two factors which may have contributed to this. The best-fit flat profile density was very sharply peaked around its optimum value, especially for chord 1, and a large number of densities was tried. In contrast, only six values of the FRANTIC edge density were available, and so a similarly-sharp optimum may have been missed. In addition, the chord 5 fit to FRANTIC distribution favored an edge

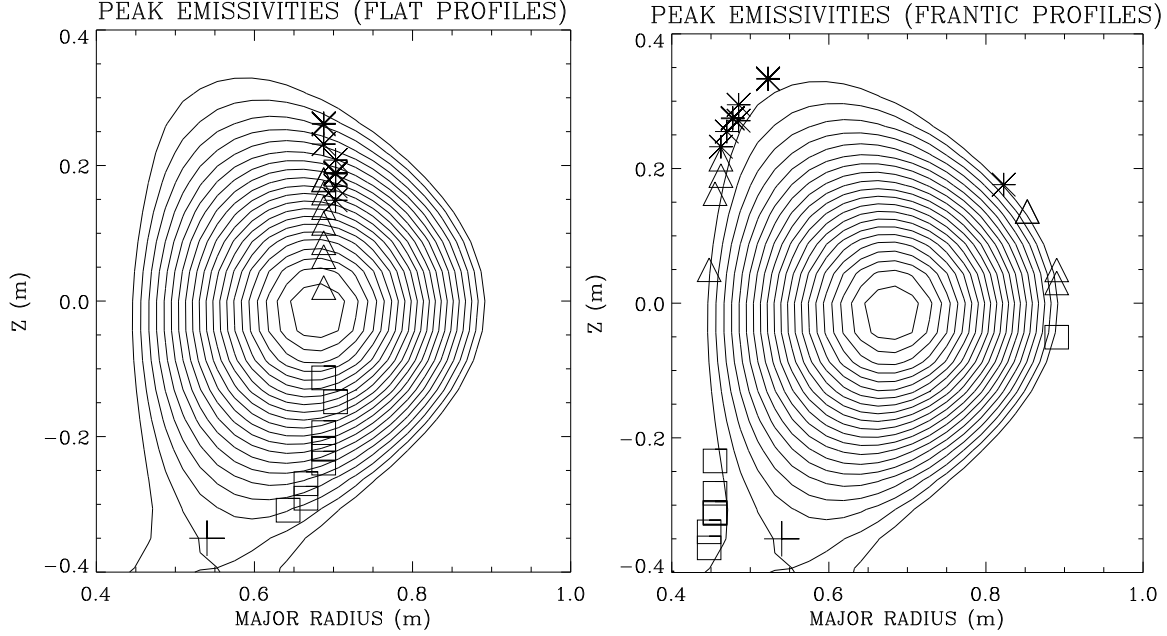


Figure 4-6: Locations of maximum charge exchange signal for the best fits to each chord position. Chords 1, 4, and 5, are plotted with squares, triangles, and asterisks, respectively.

density lower than the range available, so having a broader range of FRANTIC profiles available may affect both the split-FRANTIC and the FRANTIC-cloud optima.

3. The results of chord 4 are somewhat confusing. The densities predicted by chord 4 from each of the three models are too high to be in accord with a monotonically increasing density from the top to the bottom. None of the distributions provide a good fit for the chord 4 data, yet without it, the top and the bottom of the distributions in each model become decoupled. For instance, spectra from the top of the tokamak (chord 5) did not play a significant role in optimizing the shape of the cloud in the FRANTIC-cloud model, and the resulting cloud has a suspiciously broad distribution. Data from other diagnostics such as the Neutral Particle Analyzer and the H_α diagnostic on Alcator C-Mod suggest that neutrals are indeed concentrated strongly around the edge of the plasma, yet the chord 4 spectra do not reflect this. In fact, if they are taken into account in optimizing the FRANTIC-cloud distribution, the best-fit cloud width becomes 60 cm rather than 30 cm. One possible cause of these discrepancies is a suspected nonhomogeneity in the sensitivity of spectrometer 4, although the signals from chord 4 are generally vastly stronger than those directed more towards the edges of the plasma.

Several positive conclusions also arise from the results:

1. The hypothesized enhancement of $[H]$ near the bottom as compared with the

Table 4.2: Quantity of data from 3 chords and 11 plasma discharges, tabulated according to shot and n-level. The number in parentheses is the percentage of data for which the difference in Equation 3.7 was negative.

	By n-level			By chord number for $n = 10$		
	8	9	10	1	4	5
with $\frac{1}{n^3}$ assumption	19 (53%)	19 (32%)	30 (20%)	11 (9%)	8 (13%)	11 (36%)
with fiducial integration	19 (21%)	19 (26%)	30 (10%)	11 (9%)	8 (13%)	11 (18%)

top was confirmed. This enhancement appears to be a factor of 20 in the case of the split-FRANTIC profiles and a factor of only 3 in the case of the flat profiles; this discrepancy is likely due to the large fraction of the charge exchange signal which comes from the hot, Ar^{17+} -rich core in the case of the flat profile. Unfortunately the one-dimensional profiles in Figure 4-5 do not clearly offer a more detailed shape for this asymmetry; however, the success of the flat profile and the broadness of the optimized cloud profile suggest that the core neutral density may be higher than that predicted by FRANTIC.

2. The emissivity integration for the fiducial line (see Section 3.2) replaced a $1/n^3$ assumption used in previous work. This correction systematically lowered the calculated non-charge-exchange contribution to spectral signals, and significantly improved the quantity of useable data (Table 4.2).
3. The vertical coordinates of peak emissivity in each chord correlated very well with a more crude measurement of chord location: the Z -coordinate where the chord passes beneath the plasma center. Figure 4-7 shows this correlation in the cases of flat and FRANTIC profiles. The flat profiles agree very closely because the peak emissivities are always central; however, there is mostly good qualitative agreement even for the FRANTIC fits, which corroborates the simpler methods used previously for deducing one-dimensional profile shapes.

All of the discharges used for this work were diverted. A study of a similar set of data from limited plasmas could be very useful in determining the suitability of the FRANTIC-shaped distribution, since the reasons to expect a divertor-region H cloud and an up-down asymmetry would be essentially absent.

Another valuable step would be to simply be able to run the tokamak with a higher central temperature; this would boost the charge exchange signals considerably by providing more Ar^{17+} for transport to the edge. In addition, a greater variety and number of view chords would better enable the deconvolution of the neutral hydrogen profile, and could in particular be useful for discriminating between the two distinct qualitative possibilities shown in Figure 4-6.

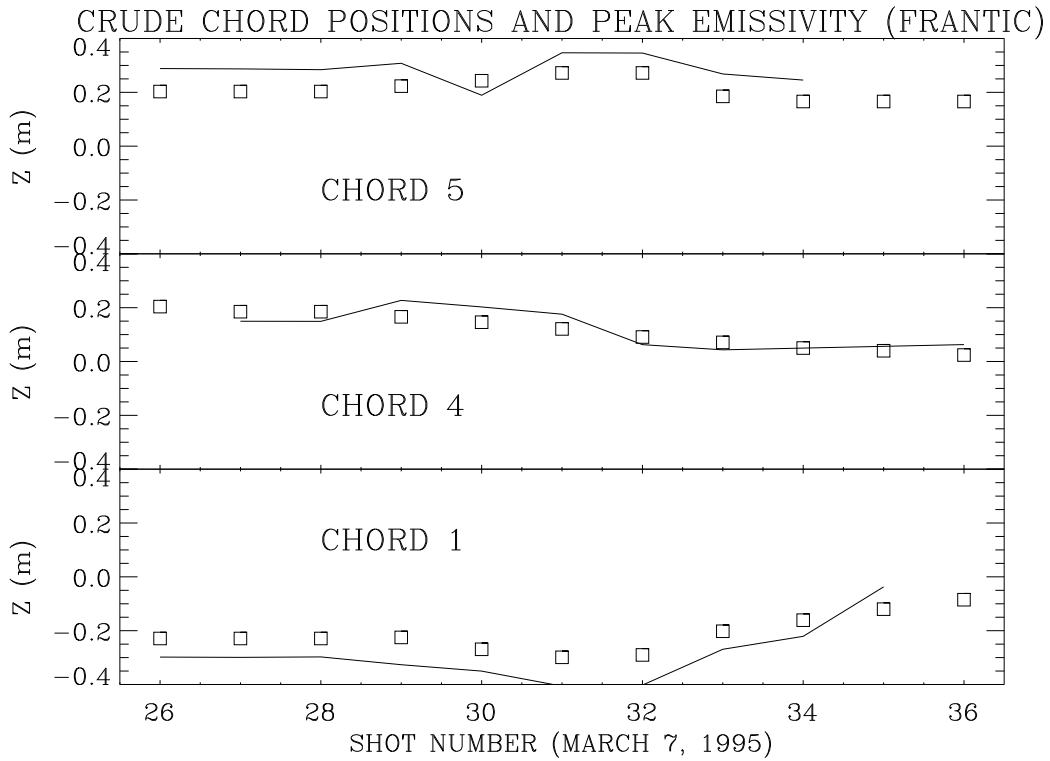
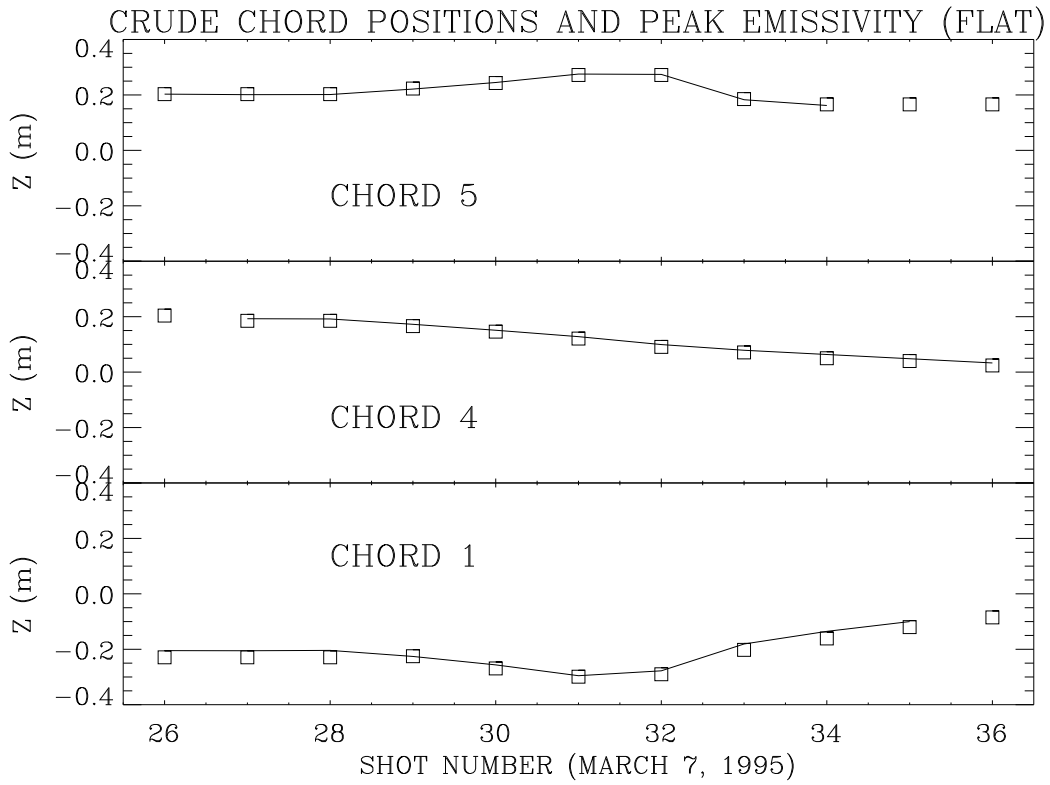


Figure 4-7: Correlation between a simple measurement of chord position (squares) and the location of peak emissivity (solid lines).

Chapter 5

Summary

In this study the spatial distribution of neutral hydrogen has been examined for a series of identical tokamak discharges containing puffed argon. The spectral line contribution due to charge exchange recombination between Ar^{17+} and neutral hydrogen was determined by comparison of brightnesses from different spectral lines. A rough deconvolution of the neutral hydrogen profile was then attempted by integrating these contributions along the plasma volume contributing to each spectrometer response, and comparing the result with experimental observations.

A number of assumptions made in previous studies [2, 3] was relaxed in this work:

- A $1/n^3$ dependence of $\langle\sigma v\rangle_{EXC}^{n^1P}$ and $\langle\sigma v\rangle_{RR}^{n^1P}$ was not assumed; to assess the fraction of charge exchange signals, emissivity integrals were carried out along each viewing chord for both a fiducial line and a line populated by charge exchange.
- The spectral brightnesses were not assumed to come primarily from the centermost point in each viewing chord, but rather the entire length of the chord inside the plasma was taken into account; however, results suggested that the one-dimensional approximation is reasonable based on the spatial emissivity profiles.
- Possible forms of the neutral hydrogen density profile other than that predicted by FRANTIC were considered; in particular, the density of neutrals was not assumed to be a function solely of the radial flux coordinate.

In addition, the data reviewed in this study were markedly more extensive and consistent than those which have previously been available.

Three shapes of two-dimensional neutral hydrogen profile motivated by theoretical considerations and each containing two degrees of freedom were tested against the set of observed data. In each case the comparison with observed spectra suggested the existence of a significant enhancement of neutral hydrogen density at the bottom of the tokamak, near the divertor region and X-point of the plasma, where ions are known to recombine after they escape the last closed flux surface of the plasma.

Although the experimental observations and numerical procedure used were detailed enough to differentiate between the three proposed models, several features of

the results indicate that a lot more data would be required to perform a more precise deconvolution of the neutral density profile. For practical reasons, this will necessitate the consideration of other plasma diagnostics than HIREX alone.

Appendix A

Charge Exchange Recombination Rate Coefficient

Recalling Equation 2.9 for the rate coefficient for charge exchange recombination between Ar^{17+} and neutral hydrogen into level n ,

$$\langle\sigma v\rangle_{CX}^n = 2.2 \times 10^{-14} e^{-(n-9.1)^2} T^{0.39} \text{ m}^3/\text{s}.$$

A qualitative justification for the preference for charge exchange into level $n = 9$ using purely classical ideas is as follows.

Consider a Bohr hydrogen atom in its ground state, and a Bohr hydrogen-like Ar^{17+} ion also in its ground state. The energy of the hydrogen's electron is just the Bohr energy,

$$E_1 = -13.6\text{eV}.$$

The electron in the inner orbital of the hydrogen-like argon ion has a screening number of 1.0 for orbitals n where n is considerably greater than 1. Thus the energy of these orbitals is

$$E_n^{\text{Ar}^{17+}} = E_1 \frac{(18 - 1.0)^2}{n^2},$$

and thus the $n = 17$ level has exactly the same energy as the hydrogen atom's electron:

$$E_{17}^{\text{Ar}^{17+}} = E_1 \frac{(18 - 1.0)^2}{17^2} = E_1.$$

The radius of the hydrogen electron orbital is a_0 , the Bohr radius. The radius of the $n = 17$ orbital of Ar^{17+} is

$$r_{17}^{\text{Ar}^{17+}} = a_0 \frac{17^2}{18}.$$

When the hydrogen atom and the Ar^{17+} ion collide, they approach each other without repulsion (since the hydrogen atom is neutral). When they reach a mutual distance of $a_0 + r_{17}^{\text{Ar}^{17+}}$, the hydrogen's electron finds itself in either the hydrogen $n = 1$ level or the Ar^{17+} $n = 17$ level, since they have the same energy and now overlap. If the electron then transfers to the Ar^{17+} ion, it leaves a proton H^+ and an argon ion Ar^{16+}

with one electron excited to $n = 17$, and the two species are a distance

$$r_i = a_0 + r_{17}^{\text{Ar}^{17+}}$$

apart.

There is now an electrostatic repulsion between the proton and Ar^{16+} with energy

$$E_c = C \frac{16e^2}{r_i^2}.$$

If, as the two particles move apart, the argon's excited electron takes up the energy E_c , it would end up in an orbital with energy

$$E_f = E_1 - E_c$$

if such an orbital were to exist.

Evaluating E_f :

$$a_0 = 0.5292 \times 10^{-10} \text{ m}$$

so

$$E_f = E_1 - C \frac{16e^2}{r_i^2} = -39.07 \text{ eV}.$$

But this, by fortune, corresponds to a level $n \approx 9.03$ since level $n = 9$ has energy

$$E_9^{\text{Ar}^{17+}} = E_1 \frac{(18 - 1.0)^2}{9^2} = -39.30 \text{ eV}.$$

Bibliography

- [1] Hans A. Bethe and Edwin E. Salpeter. *Quantum Mechanics of One- and Two-Electron Atoms*. Plenum Publishing Corporation, New York, NY, 1977. [10](#), [11](#), [12](#), [13](#)
- [2] J. E. Rice et al. “radial profiles of ground-state transitions of heliumlike argon from the alcator-c tokamak”. *Physical Review A*, 35(7):3033–3045, April 1987. [13](#), [16](#), [20](#), [24](#), [25](#), [26](#), [39](#)
- [3] J. E. Rice et al. “observations of alcator c-mod plasmas from a five chord high energy resolution x-ray spectrometer array”. *Rev. Sci. Instrum.*, 66(1):752–754, January 1995. [8](#), [16](#), [17](#), [20](#), [22](#), [26](#), [39](#)
- [4] Robin M. Hochstrasser. *Behavior of Electrons in Atoms*. W. A. Benjamin, Inc., New York, NY, 1964. [12](#)
- [5] R. C. Isler. “impurities in tokamaks”. *Nuclear Fusion*, 24(12):1599–1669, 1984. [13](#), [14](#), [15](#), [19](#)
- [6] R. Mewe. “interpolation formulae for the electron impact excitation of ions in the h-, he-, li-, and ne-sequences”. *Astron. Astrophys.*, 20:215–221, 1972. [19](#)
- [7] R. Mewe and J. Schrijver. “heliumlike ion line intensities”. *Astron. Astrophys.*, 65:99–114, 1978. [15](#), [18](#), [19](#)
- [8] D. S. Belic R. K. Janev and B. H. Bransden. *Phys. Rev. A*, 28:1293, 1983. [19](#)